Shock Wave / Boundary Layer Interaction Experiment on Control Surface

Stefan Schlamp, Lukas Prochazka and Thomas Rösgen
ETH Zürich, Institute of Fluid Dynamics
Sonneggstr. 3, 8092 Zürich
Switzerland

schlamp@ifd.mavt.ethz.ch / prochazka@ifd.mavt.ethz.ch / roesgen@ifd.mavt.ethz.ch

ABSTRACT

The shock wave / boundary layer interaction (SWBLI) experiment is part of the EXPERT mission. SWBLI is studied on two identical fixed compression ramps made of C/SiC, which are models for control surfaces. The flow separates on the flat surfaces upstream of the compression ramps and reattaches on the ramp surfaces. A reattachment shock results, which interacts with the boundary layer.

One ramp is instrumented with thermocouples. An infrared camera (InGaAs detector array) views the inside of the second flap. A 50 nm bandpass in front of the detector extends its temperature measurement range to over 2,000 K. This provides temperature maps with a spatial resolution of O(1 mm) at 30 Hz. The heat flux on the flap's exterior is obtained from the temperature distribution history and the known thermal properties of the structure using an inverse method.

The locations of the detachment and reattachment shocks are very sensitive to numerical errors and changes of the flow conditions. This flow phenomenon is thus highly suitable to validate numerical results and to examine if and how wind tunnel results can be extrapolated to re-entry flows.

The status quo of the payload design is described; CFD and FEM results are presented.

1.0 INTRODUCTION

The challenges in designing in-flight space of re-entry experiments are different from those for ground-based experiments. While the ultimate objective – to obtain data with the highest possible accuracy – is the same, the constraints posed by the vehicle size, mass, mechanical loads, thermal loads, power, data storage and experiment control, to name just a few, typically mean that techniques, which are considered standard in a laboratory setting are state-of-the-art for flight experiments. Also, a new measurement technique goes along with new hardware, which has to be customized and qualified for space applications. This is a lengthy (and risky) process and is partly to blame for the lag between when a technique could be applied to in-flight tests (*i.e.*, when all necessary components are available to meet the requirements and constraints mentioned above) and when it is actually applied. Another contributor is the lack of launch

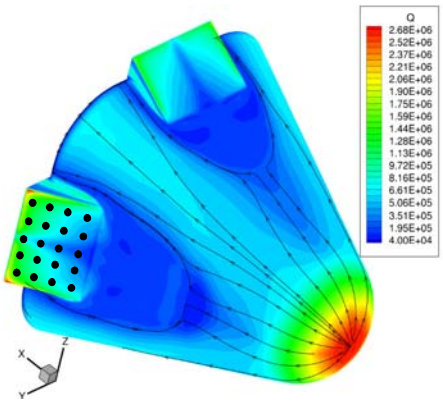

Figure 1: EXPERT vehicle with four ramps. Color-coding reflects numerical results of the surface heat flux.

Schlamp, S.; Prochazka, L.; Rösgen, T. (2007) Shock Wave / Boundary Layer Interaction Experiment on Control Surface. In *Flight Experiments for Hypersonic Vehicle Development* (pp. 14-1 – 14-22). Educational Notes RTO-EN-AVT-130, Paper 14. Neuilly-sur-Seine, France: RTO. Available from: http://www.rto.nato.int/abstracts.asp.

opportunities to evaluate innovative experiments.

In this paper we describe the status quo of one experiment expected to participate in ESA's EXPERT (Experimental Re-entry Testbed) mission set to launch in 2007. The remainder of this chapter will give an introduction to the overall mission and its objectives, to the flow phenomenon under investigation and the measurement technique employed. Chapter 2 will then discuss the design of the payload in greater detail and give the rational for some of the design decisions and component choices. Chapter 3 will then address the payload integration into the vehicle and cover the issues related to the environmental conditions during the mission. The proposed post-flight data analysis is presented in Chapter 4. A summary and possible payload extensions for future flights are presented in Chapter 5.

1.1 EXPERT Mission

The objective of EXPERT is to obtain data from a number of different payloads to validate numerical results and to examine whether (and how) or not wind tunnel results can be extrapolated to match experimental results. Current plans include two flights with different re-entry trajectories (5 and 6 km/s) lasting approximately two minutes each. The capsule will be launched on a ballistic missile from a Russian submarine and land under a parachute on the Kamtchatka peninsula, where the data recorder and possibly the entire vehicle will be recovered. During re-entry, the vehicle's yaw and attitude are controlled by thrusters to within 0.5° thereby creating a flow field, which is symmetric with respect to the symmetry planes of the capsule. The shape of the capsule and the objectives are similar to DART (Delft Aerospace Re-entry Test demonstrator) from Delft Technical University. Ref. [1] gives a more detailed description of the vehicle and the mission profiles.

In order to distinguish between different turbulence or chemistry models, for example, high-fidelity experimental data is required. It is most suitable to measure quantities which are very sensitive to errors in the numerical setup or flow conditions. Figure 1 shows the basic layout of the EXPERT vehicle. The shock-wave/boundary layer interaction (SWBLI) experiment is located on two flat wedges on opposite sides at the tail of the capsule. Both flaps have the same angle of attack and thus provide the opportunity to build a payload with redundant measurement techniques. Note that the angle of the flaps is fixed. They can be seen as models of control surfaces for future hypersonic and re-entry vehicles. The surfaces upstream of the flaps are flat.

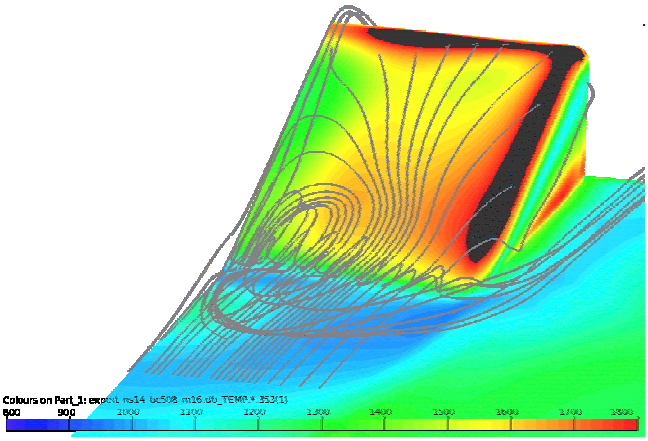

Figure 2: Path lines for 3d compression ramp flow; provided by Jan Vos, CFS Engineering.

The payload is a joint effort of the experimental, numerical and industrial communities. The project lead rests with the company HTS AG located near Zurich. HTS is responsible for procurement, mechanical design, manufacturing, integration, and qualification of the payload. The pre-flight CFD calculations needed for the payload design are performed by CFS Engineering in Lausanne/Switzerland. ETH's task is the design and layout of the measurement components and their calibration in pre-flight wind tunnel tests. ONERA developed a data analysis method [2], which will be employed for the post-flight data analysis. SNECMA finally will supply the C/SiC flaps with integrated thermocouples. The Belgian company Xenics supplies the customized infrared camera.

1.2 Shock wave boundary layer interaction

Shock-wave/boundary layer interaction (SWBLI) denotes the influence of a shock wave incident on or originating from a boundary layer. The boundary layer alters the boundary condition for the shock wave, which in turn causes large pressure gradients which couple back onto the boundary layer flow. SWBLI cannot be modelled by a superposition of a shock wave and boundary layer flow. The coupling between both phenomena is highly nonlinear [3].

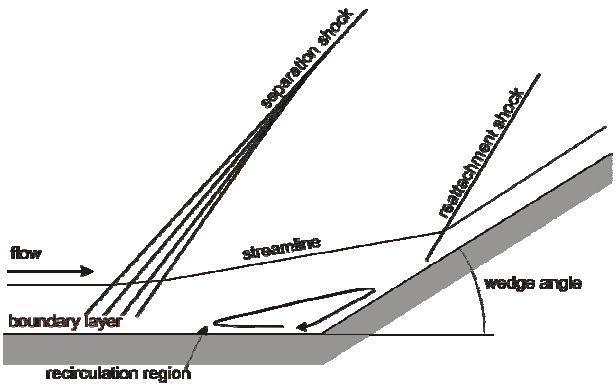

Figure 3: Schematic of flow field over a two-dimensional supersonic compression ramp.

The boundary layer spreads the usually almost discontinuous pressure jump in the shock wave over tens of boundary layer thicknesses such that the presence of the shock wave is felt upstream of the shock location. The sudden pressure jump can, for example, lead to flow separation, additional drag and increased local heat loads. It has a strong influence on the flight performance and design requirements of hypersonic vehicles. Of particular importance are the engine inlets [4], where SWBLI has a direct influence on the engine performance. Even in non-reacting flows, SWBLI is a difficult problem to study, but the addition of flow chemistry makes it one of the benchmark problems for verification and validation of numerical schemes in hypersonics [1][5][6][7]. Experiments have shown that the flow behind the shock wave contains Görtler vortices and hence is intrinsically three-dimensional [7]. Lee and Wang [8] observe that the separation shock upstream of a compression ramp oscillates, which introduces unsteady phenomena into the SWBLI problem under investigation here. The bow shock wave upstream of the ramp will likely experience similar oscillations (Figure 1). Various other groups have also performed numerical [9][10] and experimental [11][12][13][14][15][16] studies of hypersonic SWBLI. This list of references is not exhaustive, but demonstrates that a large body of numerical and wind tunnel data exists for comparison.

On the EXPERT mission, SWBLI in studied using the reattachment shock which forms on the ramps. The flow separates behind the bow shock waves upstream of the ramps (Figure 3). Figure 1 shows the stagnation streamline on the surface of the capsule going around the ramp. The recirculation region is also clearly visible in Figure 2. Figure 2 also gives an impression of the three-dimensional nature of the flow field. Of particular interest is the location of the reattachment shock as well as the spatially and temporally resolved flow field behind it and on the remainder of the ramp. The flow over the flaps is three-dimensional. The reattachment shock will form a curve over the flap surface, originating approximately from the upstream corners.

1.3 Infrared Thermometry

Without flow seeding (which was ruled out to avoid contamination of other payload experiments) and without optical access to the outside (which would not be qualifyable within the ambitious schedule), imaging techniques have to rely on information from the inside of capsule's outer shell. Infrared thermography was identified as most promising technique.

The widespread use of infrared imaging for a variety of applications suggests that the integration of this technique into a space environment should be straight-forward. The difficulties lie in the environmental conditions (vibrations and high temperatures), lack of cooling capabilities, high data rates and storage

requirements, and in the quantitative conversion of the camera data into temperatures.

An infrared camera observes the inside ramp structure. From the known optical properties of the material, the camera, and the optical setup, the temperature can be deduced. From the temperature distribution on the inside of the ramp structure and with the known optical and thermal properties of the structure, the external heat fluxes can be calculated (see Sec.1.4).

1.4 Inverse Method

For design purposes, the inside temperature is not of particular interest, because a) a thermal protection system (TPS) usually covers the inside of the structure and protects the on-board instrumentation and b) the temperature depends strongly on various factors. Of greater importance are the outside heat fluxes, which govern the design of the thermal protection system.

The derivation of the outside heat flux based on the inside temperature transients belongs to the class of inverse problems. In the context of heat flux and temperature it is referred to as the inverse heat conduction problem (IHCP). It belongs to the subclass of so-called boundary inverse problems. Inverse problems are widespread in science and technology; tomographic image reconstruction also belongs to this class of problems.[1]

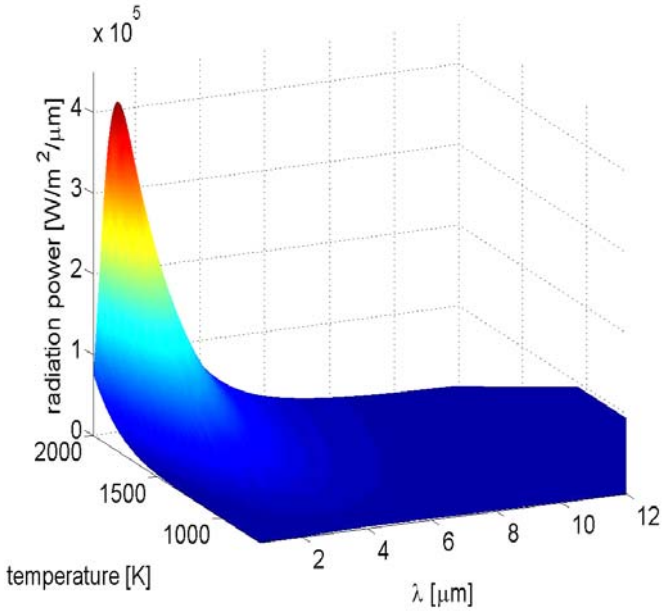

Figure 4: Radiated power as a function of temperature and wavelength according to Planck's law (Eq. 1) for a black body.

Normally the heat flux on one surface (*i.e.*, the cause) is known and one wants to calculate the temperature on the other side (*i.e.*, the effect) of the structure. The solution to this direct problem is straight-forward. The inverse problem poses some difficulties. For example, it is not stable with respect to changes of the initial and boundary conditions, *i.e.*, small changes of the temperatures can correspond to large variations of the temperature gradients [17]. Conceptually, the solution of the inverse problem works as follows:

1. Assume a heat flux distribution on the outside of the ramp
2. Solve the direct problem for the temperature distribution on the inside of the ramp structure
3. Calculate some form of error metric from the result and the actual temperature distribution
4. Modify the assumed heat flux distribution
5. Repeat steps 2 through 4 until the scheme has converged sufficiently

For 2d temperature and heat flux distributions, the parameter space is very large and the computational costs following a brute force approach are not acceptable. Nortershauser and Millan [1] devised an algorithm, which adapts strategies from image compression algorithms. Instead of treating each data point as free parameter, the image is transformed into the spectral domain and only the most relevant

[1] Tomography is a special case in that efficient algorithms (namely the Radon integral transform) exist.

frequencies are solved for. Only a small fraction of the spectrum is needed to achieve a reasonable representation of an image or, for the IHCP, of the heat flux distribution.

2.0 HARDWARE CONSIDERATIONS

2.1 Payload overview

Figure 1 is an external view of the entire capsule. Two (of the four) flaps on opposite side are allocated for the SWBLI experiment payload. One flap will be instrumented with thermocouples and possibly pressure transducers, while the second flap will be instrumented with an infrared camera. This second flap will also contain a few thermocouples for calibration purposes and to verify the symmetry of the flow field. Figure 12 shows the allocated volume inside of the capsule in light green. The capsule contains a central power supply and data handling unit (DHU). The DHU amplifies, digitizes and records the experimental data from all payloads in addition to some "housekeeping" signals. It also sends experiment control signals to the payloads. The allocated payload volumes thus have to house only payload-specific equipment.

Type B (usable to 1,768ºC sustained) or type S (usable to 1,704ºC sustained) thermocouples will be used as classical temperature sensors. These will be integrated with the C/SiC flap using SiC clamps (Figure 16). The signal levels with these thermocouples are low (<20 mV at 1,700ºC), but given low-noise amplifiers and high-dynamic range digitizers, the measurement error and uncertainty are in the order of 0.1%. On flap 1, the thermocouples will be arranged in a matrix pattern as shown schematically in Figure 1. The thermocouple data will show when the reattachment shock passes over one of the thermocouples. Flap 2 is instrumented with only two to four thermocouples (still to be determined). They will be located at positions, which correspond to thermocouples on flap 1. This layout allows one to verify the correct attitude and yaw of the vehicle. The thermocouples will be used to validate the results from the infrared camera and to provide a few calibration temperatures.

This is necessary because the infrared camera does not measure temperatures directly, but radiated power within a specific spectral range. This depends on the optical properties of the body. The emissivity of C/SiC is temperature-dependent and is also influenced by material aging processes. It will be impossible to replicate the temporal history of the temperatures in a lab and thereby determine the emissivity of the flaps. Furthermore, the emissivity can also depend on the angle of view, which varies across the field-of-view of the camera. But using known temperatures (from thermocouples) at a small number of reference locations can provide the necessary input to convert the intensity images of the infrared camera into temperatures. The thermocouples and the clamps within the field-of-view of the camera can also be used to correct for image shifts caused by vibrations and relative displacements between the flaps and the internal structure. Depending on the location on the vehicle, these displacements can reach 20 mm. All payloads had to be attached to the base structure and the points of contact with the outer shell had to be avoided or kept to a minimum.

An infrared camera will be installed behind flap 2. Over a mirror, it will observe a large fraction of the flap. It will provide thermographic images at 30 Hz with a spatial resolution of 320 x 240 pixels and 12 bit resolution. The SWBLI experiment is the only EXPERT payload with imaging equipment. The data rates and storage requirements represent more than 95% of the overall mission. It was therefore decided to record the data not in the DHU, but on a separate payload-internal device. This payload data handling unit (PDHU) is located in the payload volume behind flap 1 (with classical instrumentation).

2.2 Mechanical Loads

EXPERT's outer shell consists of PM1000, a Nickel-Chromium alloy with traces of Aluminium, Titanium and Yttrium-Oxide. Its maximum temperature rating is 1200°C. It is resistant to atomic oxygen and has a

high emission coefficient, leading to effective radiation cooling. Compared with other metals, it has a low catalycity.

The nose and the four flaps will me manufactured from carbon-fiber-reinforced silicon carbide (C/SiC). The two closed flaps for the SWBLI experiment are supplied by SNECMA Moteurs, the two open flaps by MAN. The fiber reinforcement results in a pseudoductile fracture of the hard SiC ceramic. C/SiC is intrinsically oxidation resistant. The mismatch between the thermal expansion coefficients of the carbon fibers and the SiC matrix leads to thermal stresses and micro-cracks in the matrix until oxidizing gas can reach the carbon fibers. This process limits the lifetime of the material.

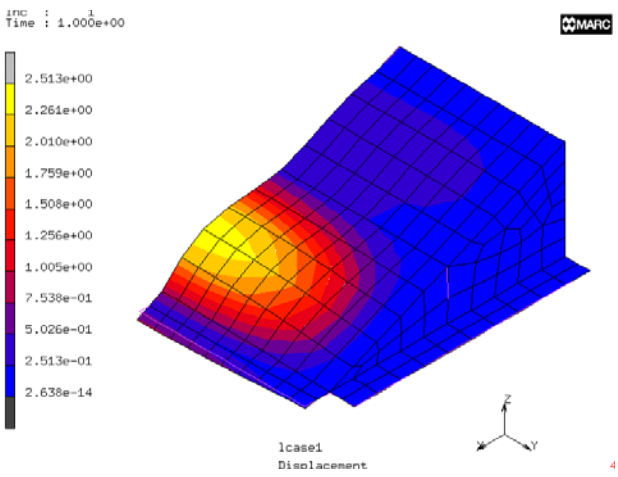

Figure 5: Finite element calculations of deflections caused by decompression shock at stage separation. Picture provided by SNECMA Moteurs.

A finite element method (FEM) study by SNECMA Moteurs (Figure 5) determined that the design-critical loads do not occur during the re-entry phase of the mission, but during stage separation of the Volna launcher. The enclosure of the EXPERT capsule (and the inside of the capsule) has an internal pressure of 0.4 bar relative to near-vacuum outside at the time of stage separation. This overpressure is needed for a successful separation, because it provides the required pushing force. This pressure is vented within a fraction of a second. As a result, the thickness of the C/SiC flaps had to be increased from 1-2 mm to 3 mm and additional stiffeners inside the flap had to be added. The stiffeners have two drawbacks: First, they partially obstruct the field of view of the infrared camera. Secondly, they increase the complexity of the structure, making the reconstruction of the external heat fluxes from the internal temperatures more difficult. The increased material thickness effectively reduces the spatial (and temporal) resolution of the measurements: Consider a Delta function-like local heat flux. Heat conductions within the structure broadens the peak such that the temperature rise on the opposite side will be approximately Gaussian. The spread increases with increasing material thickness. The non-zero heat capacity of the material introduces thermal “drag”, which distorts the temporal temperature response.

During the re-entry, thermal stresses determine the design of the attachment points of the flap. The coefficients of thermal expansion of C/SiC and PM1000 are not matched such that the fixation points at the leading edge and along the sides of the flap have to allow for lateral movement while maintaining a reasonable sealing. This movement requires a sufficiently low friction between the two materials. Unfortunately, C/SiC has a large friction coefficient at elevated temperatures such that additional measures are necessary to ensure a smooth stress balancing along the interface. The rear of the flap has two attachment points to the cold structure of the capsule (see Figure 16, left).

Vibrational and acoustical loads are relevant for electronic components. Noise levels at launch reach 160 dB and vibrational loads 30 g RMS. The components have to be qualified for these loads or have to be mounted with some vibration damping. The DHU (and PDHU) should preferably be shock resistant in case of a parachute failure.

2.3 Thermal Loads

At this point we want to distinguish between two thermal loads, namely the high (up to 2,000ºC) temperatures on the outside of the flap and the thermal environment inside the capsule, which the

electronic and optical components are exposed to.

2.3.1 External

Figure 6 shows numerical results for the surface temperatures on the flap at the point in the trajectory where maximum heating is expected. The non-equilibrium chemistry computation was only performed for a quarter of the vehicle (which has two planes of symmetry). The figure shows that the highest temperatures will occur near the sides and the trailing edge of the flaps. The temperatures reach and exceed 2,000 K in these regions. The temperatures remain below 1,700 K over most of the flap surface. Independent calculations by SNECMA Moteurs produced qualitatively similar results. These data are used as inputs for the selection of the infrared technology (Sec. 2.4).

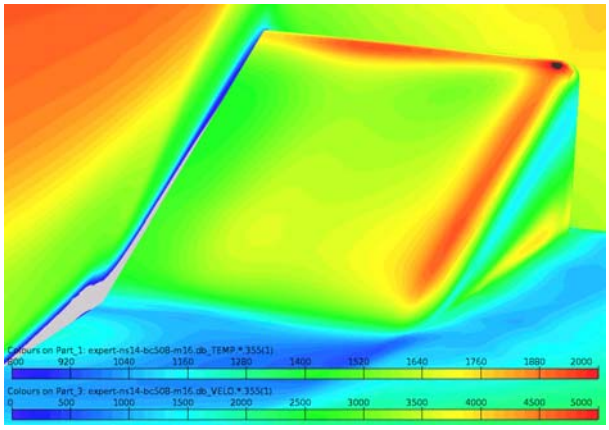

Figure 6: Surface temperature from non-equilibrium CFD calculations; provided by Jan Vos, CFS Engineering.

2.3.2 Internal

The inside of the capsule is neither pressurized nor temperature-controlled. The base structure is expected to reach 150ºC at landing. The temperature in the electronics enclosures is expected to reach 75ºC. Temperatures approaching those of the C/SiC would be observed on components which are exposed to the thermal radiation if no additional measures were taken. This requires that all electronic components have sufficiently high operating temperature ratings or that they are cooled. Heat cannot be transferred to the base structure, which is even hotter, or to the air inside the capsule, because the densities are too low during the most critical phases of the mission. This requires an additional heat sink. Sec. 3.1 discusses the use of a phase change material for this purpose.

2.4 Infrared detector

2.4.1 Overview over infrared detection technologies

Common IR detectors belong either to the class of photon detectors or to the class of thermal detectors. In the first class of detectors the radiation is absorbed within the material by interaction with electrons. The electrical signal output is derived from measurements of changes in conductivity (photoconductor) or current (photovoltaic) due to the absorbed photons (see Table 1). The second class is composed of thermal detectors. Here, the incident radiation is absorbed leading to a change of the temperature and hence some physical properties of the sensor material. Typical thermal imaging detectors are either pyroelectric devices, where the change in the internal electrical polarization is measured, or bolometers, where the resistance is changing.

Thermal detectors are typically operated at room temperature, whereas photon detectors have to be cooled – often down to cryogenic temperatures (say, 77 K). This is necessary to prevent the thermal generation of charge carriers inside of the detector material.

The spectral responsivity is given by the minimum energy gap of the material which decreases with the wavelength of the incoming radiation: the smaller the energy gap, the higher the thermal noise. As a consequence, photon detectors having a long-wavelength limit above approx. 3 µm are generally cooled.

Due to the cryogenic cooling, photon detector assemblies are usually larger, more expensive and require

more electrical power than thermal detector subsystems.

Table 1: Summary of infrared technologies considered.

	Thermal Detectors		Quantum Detectors
	Bolometer	**Pyrometer**	**InGaAs**
Working Principle	ΔR= f(T)	ΔQ= f(T)	ΔI= f(T)
Sensitivity Band	8-12 μm (FIR)	0.9-1.7 μm (NIR)	0.9-1.7 μm (NIR)
Cooling	No	No	Yes (thermoelectric)
Detectivity	+	+	++
Spatial resolution	++ (FPA)	++ (FPA)	++ (FPA)
Temporal Resolution	+	-	++
Size	++	+	-
Power Consumption	++	++	-
Cost	++	++	-
T_{max}	500 °C	> 2000 °C	< 800 °C

On the other hand, photon detectors have a faster temporal response and are much more sensitive, for example the maximum detectivity of an InGaAs photon detector is ≈ 10^{12}cmHz$^{0.5}$W^{-1}, compared to a bolometer with 10^{8} cmHz$^{0.5}$W^{-1}.

Thermal detectors are generally wavelength independent. The reason why most commercial bolometers are working in a spectral range between 8 and 12 μm is the high transmissivity of the atmosphere and the high emissivity of common materials in this spectral range. In this way, parasitic radiation contributions from a low emissivity spectral range can be avoided.

Commercially available bolometers and InGaAs detectors have a limited temperature measurement range with a maximum object temperature of about 500°C and 800°C, respectively. The measurement range can be extended with neutral density filters, band pass filters or pin holes but a decrease in sensitivity at lower temperature results.

Pyrometers are suitable for high temperature measurement, but they respond only to (temporal) changes in the incident radiation and are inappropriate for low frequency operation below 1 Hz. Most pyrometric cameras operate with an optical modulator or “chopper” to modulated the incoming radiation in order to remove offset variations between elements in the array and to eliminate long term drifts. Thus they may not be well suited for an application in a harsh environment.

The assets and drawbacks of the various sensor technologies are summarized in Table 1.

2.4.2 Wavelength selection

Every body of temperature T and emissivity ε radiates energy. The emissivity is in the range [0…1], is typically a function of the temperature, viewing angle (neglected in the subsequent treatment), and the wavelength λ, but can usually be assumed constant. The spectral energy density (energy per unit wavelength) per unit solid angle is governed by Planck’s law,

$$R(\lambda,T) = \varepsilon \frac{2hc^2}{\lambda^5} \frac{1}{e^{hc/(\lambda kT)} - 1}, \tag{1}$$

where c is the speed of light. h is Planck's constant and k is the Boltzmann constant. This relationship is plotted in Figure 4. For a given temperature, Eq. 1 has a maximum at a certain wavelength. For low temperatures, this wavelength is in the far infrared. With increasing temperature, the maximum shifts towards lower wavelengths. The total radiated power, *i.e.*, the integral of Eq. 1 over all wavelengths, increases with the fourth power of the temperature.

Both effects are favourable for the application of infrared thermography for high-temperature applications. The radiation is very strong such that uncooled detectors can be used, which can operate in the near-infrared (NIR) spectral band. This means that conventional optical materials can be used instead of germanium optics.

An infrared camera records the radiation from a certain spectral range. From the known range and the emissivity of the body under observation, the temperature can be calculated. The intensity of each pixel of the IR camera's image is proportional to

$$R_{\lambda_a}^{\lambda_b}(T) = \int_{\lambda_a}^{\lambda_b} R(\lambda,T) d\lambda . \tag{2}$$

The absolute value depends on the solid angle, which each pixel covers and the characteristics of the camera. Above approximately 1,250 K, the radiated power in the NIR exceeds that in the FIR. For low-temperature infrared thermography, signal levels are an issue, which is why room-temperature infrared cameras operate in the FIR. In the temperature range expected for the SWBLI experiment, the radiated power far surpasses the saturation limit of the cameras irrespective of the spectral band even for the shortest exposure times. Therefore, measures have to be taken to limit the amount of radiation, which reaches the detector. This can be achieved by

- a band-pass filter, which limits the spectral range to a fraction of the spectral range to which the detector is sensitive,
- a pin-hole, or
- a neutral-density filter.

A final decision has not been made, but the subsequent results are largely independent of this choice.

An important measure is the sensitivity S, which describes the change of signal (pixel intensity) per unit change of the observed quantity, *i.e.*, temperature. For an ideal detector it is,

$$S(T) = \int_{\lambda_a}^{\lambda_b} \frac{dR(\lambda,T)}{dT} d\lambda = \frac{dR_{\lambda_a}^{\lambda_b}}{dT}. \tag{3}$$

Just as for the absorbed energy, the sensitivity is several orders of magnitude lower with a NIR than with a FIR camera. Only at temperatures above 1,500 K do the two detectors show similar sensitivity.

In a real detector the sensitivity is also influenced by the capability of the detector material to detect infrared radiation and by the camera noise characteristics. The detectivity, D, incorporates these two effects. The product of the sensitivity (Eq. 3) and the detectivity is proportional to the reciprocal of the noise equivalent temperature difference (NETD), another figure of merit in infrared detector technology

(Eq. 4),

$$NETD \propto \left(S \cdot D\right)^{-1}. \tag{4}$$

The NETD is the temperature difference which would correspond to the electronic noise in the detector. It is specific for each camera model. The NETD in the NIR is below that in the FIR for T > 450 K approximately. The detectivity of an uncooled InGaAs photon detector is approximately 4 orders of magnitude higher than the detectivity of a microbolometer. This fact leads to a higher sensitivity of a real NIR compared with a FIR camera for temperatures higher than 500 K.

The contrast provides information about the capability of the camera to distinguish between the object and the thermal background radiation. It is defined as

$$C\left(T_0, T_f\right) = \frac{R_{\lambda_a}^{\lambda_b}\left(T_0\right) - R_{\lambda_a}^{\lambda_b}\left(T_f\right)}{R_{\lambda_a}^{\lambda_b}\left(T_0\right) + R_{\lambda_a}^{\lambda_b}\left(T_f\right)}. \tag{5}$$

It relates the detected radiation from the body at temperature T_0 to that thermal radiation being emitted by the background at temperature T_f. The contrast in the NIR is greater than that for the FIR by a factor of four to six for temperatures above 400 K (assuming T_0-T_f = 10 K).

The contrast, the sensitivity and the noise-equivalent temperature difference (NETD) can be combined into a quality factor Q, which provides an overall comparative figure-of-merit,

$$Q = \frac{R_{NIR}}{R_{FIR}} \cdot \frac{NETD_{FIR}}{NETD_{NIR}} \cdot \frac{C_{NIR}}{C_{FIR}}. \tag{6}$$

A quality factor greater than unity indicates that a NIR detector is advantageous. The quality factor increases rapidly with temperature. For room temperature, it is in the order of 10^{-15}. For temperatures above approximately 1,000 K, Q > 1. At 2,000 K, Q ~ 10^3. For this reason, an InGaAs detector in the NIR spectral band was chosen.

2.4.3 Noise considerations

The photodiodes in an InGaAs focal plane array are normally operated in reverse-bias mode. Due to the high impedance of the diode the shot noise due to the dark current is the dominant noise source. The dark current itself increases exponentially with detector temperature. During measurement the photo-current created by the incoming radiation generates an additional shot noise contribution. In general, the shot noise increases with integration time.

The flicker noise or “1/f”-noise that is inversely proportional to the measurement frequency becomes noticeable at frequencies below 1 Hz. For high temperature measurements the exposure times are much smaller than 1 s, so flicker noise can be neglected.

In a focal plane array additional noise is generated by the readout integrated circuit (multiplexer) as well as the external camera electronics. Readout noise increases roughly linearly in temperature and only occurs once per scan. The shot noise contributions due to the dark and photocurrent are given by

$$\left\langle I_{sd}{}^2 \right\rangle^{1/2} = \sqrt{2qBI_{dark}}\,; \quad \left\langle I_{sp}{}^2 \right\rangle^{1/2} = \sqrt{2qBI_{photon}}\,; \quad B \approx \frac{1}{2ET} \tag{7}$$

Here, q is the charge of an electron ($1.602 \cdot 10^{-19}$ C) and the measurement bandwidth B is associated with the exposure time ET. The typical dark current of an InGaAs-detector is 500 fA per pixel at 20°C. In the following calculation, a safety factor of 2 is introduced. Thus, a dark current of 1 pA was assumed. The photocurrent per pixel is given by

$$I_{photo} = \eta A_{pix} \int_{\lambda_1}^{\lambda_2} \frac{dN(\lambda,T)}{d\lambda} d\lambda\,, \tag{8}$$

where η is the quantum efficiency (for an InGaAs-detector ≈ 85%) and Apix represents the pixel area (assumption: 30x30 µm^2). The integral gives the absorbed number of photons per unit of time and area in the spectral sensitivity range of the detector.

The readout noise was assumed as 1 ADC or 600 electrons, a typical value for focal plane array as well. When the noise sources are uncorrelated, they add in quadrature, that is

$$Noise_{tot} = \sqrt{Noise_1{}^2 + Noise_2{}^2 + \ldots + Noise_3{}^2}\,. \tag{9}$$

Figure 7 shows the integrated noise created by the dark current and readout as a function of detector temperature for different exposure times. The isolated readout noise is visible as well. It can be seen that below 1 ms integration time the shot noise due to the dark current is negligible.

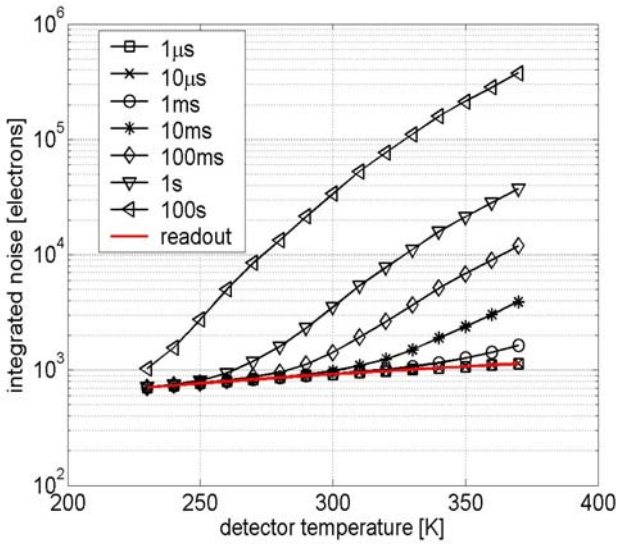

Figure 7: Detector noise as function of temperature and integration time.

Figure 8 shows the incoming radiation integrated during the exposure time and expressed in electrons. Furthermore, the resulting shot noise due to the photocurrent the readout noise and the total noise composed of the shot noise due the dark- and photo-currents and the readout noise are visible.

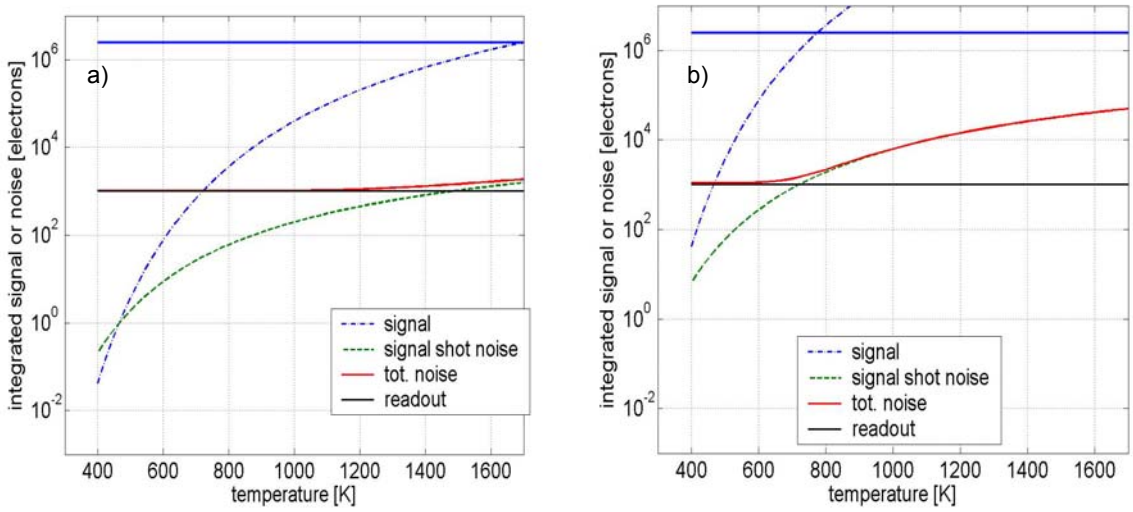

Figure 8: Integrated signal and noise contributions at 1 µs (a, left) and 1 ms (b, right) integration time. The solid blue line denotes detector saturation.

The total noise figure is based on the maximum considered detector temperature of 60°C, but especially for short integration times the dependency on detector temperature is negligible (see Figure 7). Figure 8a assumes a minimum integration time for typical NIR-cameras of 1µs whereas Figure 8b is based on an exposure time of 1 ms. At 1,700 K and 1 µs exposure time the detector is saturated. The number of 2.5×10^6 electrons represents the detector's full well capacity. To prevent a saturation at the mentioned temperature and exposure time, the incoming photon flux has to be reduced by a factor of 230. This can be realized by a small aperture (pinhole) or by a neutral density filter.

The very short integration time together with the flux reduction lead to a signal-to-noise ratio of 1 at around 750 K. Thus, a measurement of lower temperatures does not appear possible. To extend the measurement range towards lower temperatures, the integration time would have to be increased implying a reduced maximum temperature range. In case of the 1 ms integration time Figure 8b), the detector would become saturated at 800 K. For the short integration times for high-temperature measurements, the readout noise is the dominant noise source for an InGaAs detector.

In Figure 9, the change of the signal to noise ratio as a function of the object temperature is shown for different integration times between 1 µs and 10 ms. It becomes clear that – depending on the target temperature differences – the measurement performance can be significantly improved by varying the integration time.

As mentioned before the sensitivity is defined as the derivative of the Planck's Law with respect to the target temperature (Eq. 3). This definition assumes an ideal detector without any noise sources. In a real detector, the noise has an influence on the sensitivity. A common figure of merit for the sensitivity in infrared detection technology is the noise equivalent temperature difference (NETD), given by

$$NETD = \sqrt{B/A_{pix}} \left[D^* \int_{\lambda_1}^{\lambda_2} \frac{dR(T,\lambda)}{dT} d\lambda \right]^{-1} \quad ; \quad D^* = \frac{\sqrt{A_{pix} B}}{NEP}. \tag{10}$$

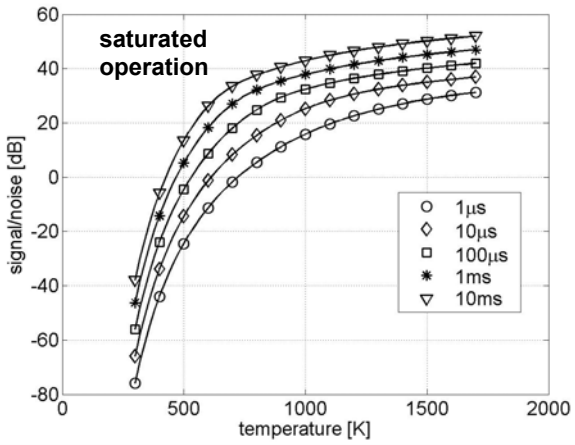

Figure 9: Signal-to-noise ratio as function of temperature and integration time.

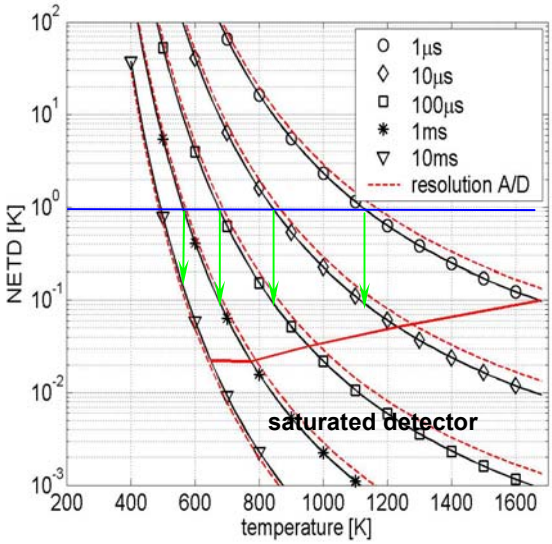

Figure 10: NETD as function of temperature and integration time.

This is the temperature difference which can just be detected above the noisy background. In the definition, D^* is the specific detectivity which is the reciprocal of the noise equivalent power (NEP), multiplied by the square root of the pixel area A_{pix} and the measurement bandwidth B to account for the dependence of the sensitivity on these two values.

The NEP is given by Eq. 11. The integral describes the radiated power at a target temperature which corresponds to a signal to noise ratio of unity.

$$NEP = A_{pix} \int_{\lambda_1}^{\lambda_2} R(T_{noise}, \lambda) d\lambda \tag{11}$$

Figure 9 shows the dependency of the NETD on the target temperature and on the integration time. The dashed lines represent the digitizing error assuming a 12 bit analog-to-digital converter and that an additional bit of resolution is lost due to noise within the converter itself. With a fixed integration time of 1 µs it is possible to detect temperature differences smaller than 1 K down to a temperature of about 1,100 K. Below 1,000 K the thermal resolution decreases rapidly. So an accurate absolute temperature measurement between 600 K and 1,700 K could be difficult without an adjustment of the exposure time.

The arrows inserted into Figure 10 indicates a strategy for integration time variation in a measurement range between 500 and 1,700 K. The criterion for the switching is the crossing of the 1 K NETD level. Obviously, the measurement range decreases for a fixed integration time with temperature. For example, the measurement range with 10 ms exposure time is around 100 K compared with a figure of around 600 K at 1 µs. Such a switching strategy is of course only valid if large temperature differences do not appear simultaneously in the camera's field of view.

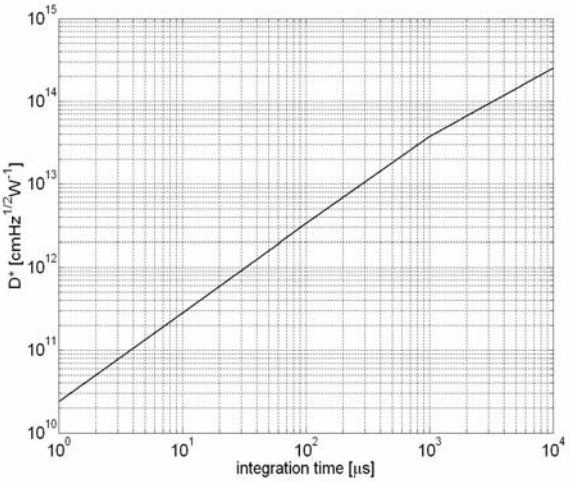

Figure 11: Detectivity as function of integration time.

Figure 11 shows the increase in detectivity with integration time. This behaviour explains the improved thermal resolution with increasing the integration time (neglecting saturation effects).

2.4.4 Conclusions

Based on the comparison of the photon detector with the bolometer regarding the capability to measure high temperatures (>1,000 K), the photon detector with an InGaAs detector can be identified as the better suited camera.

The study of the influence of the noise and integration time on the sensitivity resulted in some interesting observations.

Due to the short exposure times required at high temperatures, the shot noise due to the dark current (which increases exponentially with detector temperature) becomes very small and is thus negligible.

- The higher detector temperatures due to the absence of thermoelectric cooling should have no influence on the measurement performance.
- Due to the short integration times and the reduction of the radiation input by a pinhole aperture, the signal-to-noise ratio decreases rapidly with decreasing temperature.
- In order to enable a large temperature measurement range (500K to 1700K), a (stepwise) variation in integration time appears to be necessary.

The company Xenics has indicated the capability to build a small, uncooled InGaAs-camera with the required intelligence to control the integration time by means of a task sequencer. Its power consumption is less than 5 W.

2.5 Data Storage

The analog signals of the thermocouples will be passed to the DHU, which is not equipped to cope with the high data rates and storage requirements of the infrared camera. The data rate is

$$320 \text{ x } 240 \text{ x } 12 \text{ bit x } 30 \text{ Hz} = 3.3 \text{ MB/s} \quad (12)$$

and the total storage capacity must be

$$3.3 \text{ MB/s x } 140 \text{ s} = 461 \text{ MB}.^{2} \quad (13)$$

Furthermore, a suitable data interface (USB or FireWire) is not available on the DHU. It was therefore decided to include a payload-internal data handling unit. It is a PC104 standard based micro-computer with an ultra low power Transmeta Crusoe processor. The unit is fanless, ruggedized and has a maximum operating temperature of 85 ºC. The motherboard is equipped with FireWire and USB interfaces. At 600

[2] The original design included a visual camera with 1024 x 640 pixels for lifetime imaging phosphor thermography in addition to the infrared camera. The combined data rate exceeded 30 MB/s and the combined storage requirement was over 4 GB. The PDHU can handle these values if future flights include the thermographic phosphor thermography experiment.

MHz clock speed, the power consumption is less than 3 W. Note that shielding against cosmic radiation is not required for a mission of 2 minutes.

Attached to the motherboard is an 8 GB solid-state hard-disk with 40 MB/s sustained write speed and 85ºC maximum operating temperature. This model is used in fighter jets and it is shock qualified to 1,500 g (MIL-STD-810F) and vibration qualified up to 16.3 g RMS (20…2,000 Hz, 3 axes; MIL-STD-810F). There is no data loss after a loss of power.

The PDHU is located in the instrument compartment behind flap 1 (thermocouple flap).

3.0 PAYLOAD INTEGRATION

The SWBLI experiment is not so much a science problem but rather an engineering problem. This means that the measurement technique is well understood and that all components exist. The challenge is to integrate the payload into the system as a whole.

Figure 13 is a schematic view of the instrumentation of flap 2 from an earlier design phase. At this point in time, it was planned to use thermographic phosphors as supplementary measurement technique [6][18][19][20]. The light red camera in the front and a xenon flashlamp located just behind it are part of this effort. Also note that a gap-heating experiment (purple slit at the leading edge of the flap) is no longer part of the design. The infrared camera is shown in red together with its field of view. It looks at the flap over a mirror (light blue). The light blue box mounted on the base plate (dark blue) contained the power supply of the xenon flashlamp and is also no longer part of the design.

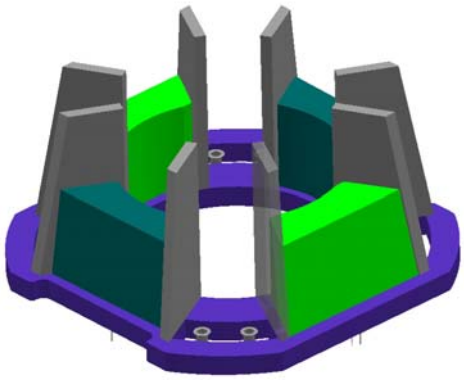

Figure 12: Allocated volume (light green) for SWBLI experiment inside the capsule. The base plate is colored blue, the base structure is grey. The parachute is located above the circular opening in the base plate.

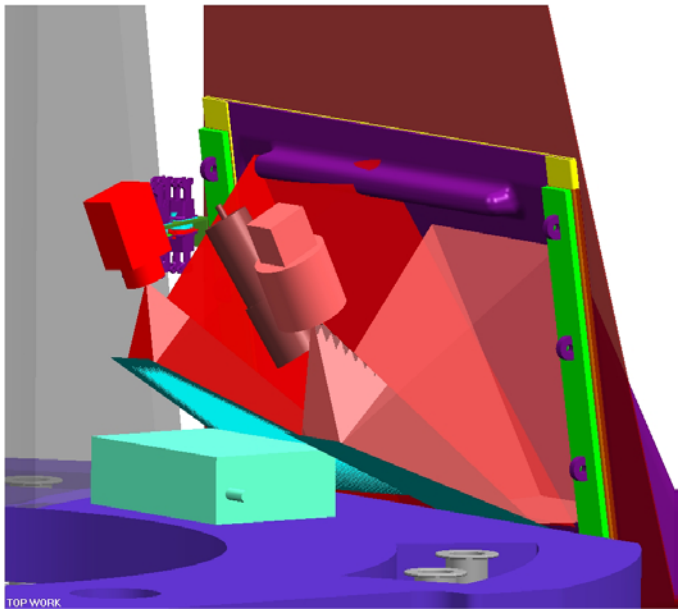

Figure 13: Integrated setup containing camera (left in red) and imaging mirror (light blue). The pink camera in front is sensitive in the visual spectral range. Together with the flashlamp (purple), it was intended for thermographic phosphor fluorescence lifetime thermography.

3.1 Thermal Management

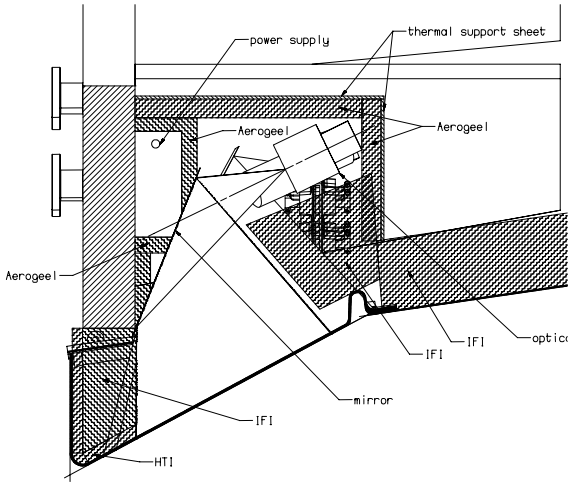

Figure 14: Optical setup and radiation shielding of infrared camera; picture provided by HTS AG.

The interior of the capsule is covered with a several centimetre thick thermal protection system. This would defeat the purpose of the infrared camera, which needs a clear view of the C/SiC flap. The inside temperature of the C/SiC will not deviate significantly from the outside temperature (Figure 6) and special measures have to be taken to protect the camera, and capsule interior from the thermal radiation emitted by the flap towards the inside.

This is demonstrated in Figure 14. Aerogel, an extremely light material with very low thermal conductivity, occupies a large fraction of the volume, which is not in the field of view of the infrared camera. The full spectral range of the radiation emitted by the flap far exceeds the damage (and saturation) threshold of the camera. A band-pass filter is thus used to restrict the spectral band to a wavelength range of 50 nm width. There are two options of how to realize this filter effect: a) by a band-pass filter between mirror and camera – all other wavelength should be reflected back to the flap - and b) by a special mirror coating, which only reflects in the desired spectral range - and absorbs or transmits the other wavelength.

For both scenarios, the mirror or filter would absorb a non-negligible fraction of the undesired radiation and thus heat up. A cooling mechanism has to be incorporated. The capsule's main structure reaches 150ºC by the time of landing and during the most critical period of the re-entry trajectory, the density is too low to dump sufficient heat into the ambient air. The current design employs phase change material (PCM) as heat sink, which is in thermal contact to the mirror, filter, and possibly also the camera.

PCM work like ice cubes do in water. When heat is added to the water/ice mixture, ice melts, but the temperature of the mixture remains at 0ºC until all the ice has melted. The heat is transferred into the latent heat associated with the phase change. PCM are available for a range of phase change temperatures. They are initially solid and melt when a certain temperature is exceeded. By cooling they can be solidified again. Table 2 gives the thermal and physical properties for a PCM with a phase change temperature of 48ºC.

Table 2: Thermal properties of phase change material.

Phase change temperature	48ºC
Maximum temperature	80ºC
Storage capacity 35 - 65ºC	93 Wh/kg
Latent heat of fusion	63 Wh/kg
Specific heat appr. in PCM	1 Wh/kg/K
Thermal conductivity	0.5 – 0.7 W/m/K

This PCM would maintain a temperature of 48ºC until it is completely melted. Based on Planck's law (Eq. 1), the expected flap temperatures, the maximum allowable temperature of the optics, an estimate of the absorption coefficient, and the cross section of the optics, the required heat capacity can be calculated. In the present design, a few hundred grams of PCM are required. Three thermocouples will monitor the temperature of the camera, the mirror, and the PDHU and transmit the data to the DHU for post-flight analysis.

Table 3 shows results obtained by HTS from a thermal analysis of the integrated payload. It shows the temperature increase of various payload components over the course of the re-entry trajectory. The flap temperature was assumed constant – a conservative estimate.

Table 3: Results from numerical analysis of thermal loads.

Part	Initial temp. [ºC]	Final temp. [ºC]
Camera	40	50
Thermal protection system	800	1750
Flap (boundary condition)	2,060	2,060
Camera support beam	40	90
Structural walls	40	49
Parachute wall	40	75
Mirror (without sink)	40	65
Mirror (with sink)	40	48

3.2 Mechanical Integration

The mechanical integration faces three challenges, two of which are solved at this point:

First, ideally one would want to mount the infrared camera at a large distance behind the flap. This reduces the amount of radiation reaching the camera, it reduces the image distortions within the field-of-view and it results in a nearly constant distance between camera and the entire field-of-view. The current design employs a mirror in combination with a wide-angle optic to view the flap under a large angle. This maximizes the field-of-view, but requires a large depth-of-field, such that no region of the flap image is blurred. Our optical analysis shows that the depth-of-field of our design is sufficient. Image distortions due to the viewing angle will be corrected in the post-flight analysis using the known geometry and a few reference points within the field-of-view.

Second, the DHU is located just above the parachute bay. On the ground, its memory can be retrieved by reaching into the now (hopefully) empty parachute bay. It is not clear if the entire capsule can be recovered. The DHU with the data is given top priority. Since the SWBLI payload utilizes its own DHU, it should also be easily recoverable. HTS designed a slide mechanism (Figure 15) to remove the hard disk drive with a single grip.

Finally, a structural analysis of the entire vehicle by Dutch Aerospace showed that significant strengthening elements are required along the circumference of the capsule. These would obstruct the

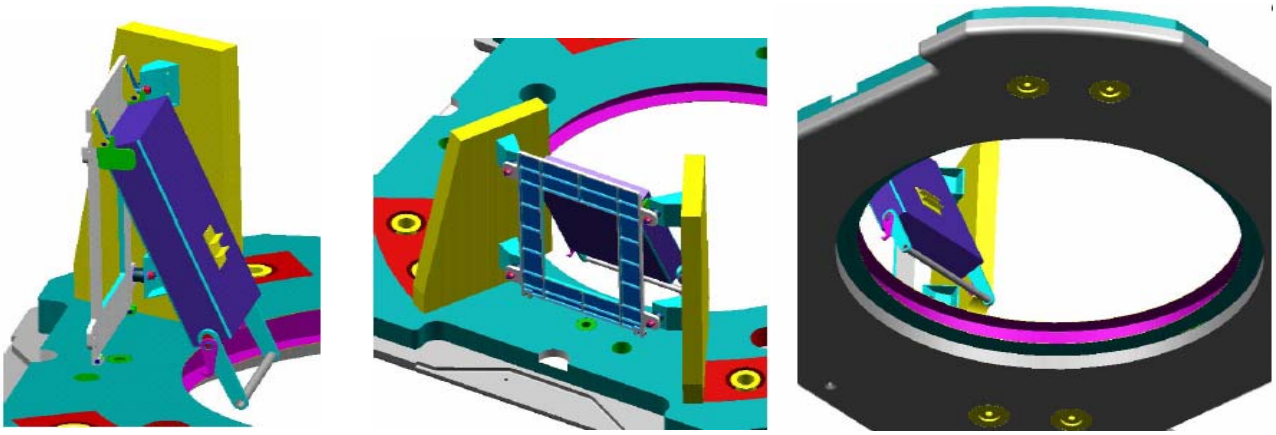

Figure 15: Slide mechanism for retrieval of payload data recorder; pictures provided by HTS AG.

field-of-view of the camera. Solutions to this issue will be addressed at the final design iteration between the SWBLI payload and Dutch Aerospace.

Figure 16 shows the C/SiC flaps with a stiffener spanning across the inside. In a further design iteration, this stiffener will be aligned with the viewing angle of the camera as to minimize the blockage of the field of view. The thermocouples are held in place by SiC clamps (blue). Figure 16 also shows the attachments of three pressure ports leading to pressure transducers. These pressure transducers are likely to be dropped from the final design.

Figure 17 shows results of a FEM calculation of the thermal expansion of the flap. The maximum relative displacement is 0.35 mm. The fixation of the C/SiC flaps to the PM1000 around the flaps is accomplished by 6 mm C/SiC screws. The PM1000 deflects below the flap overlap.

4.0 DATA ANALYSIS

The raw data consists of a series of grey-scale images and a mapping, which assigns an integration time to

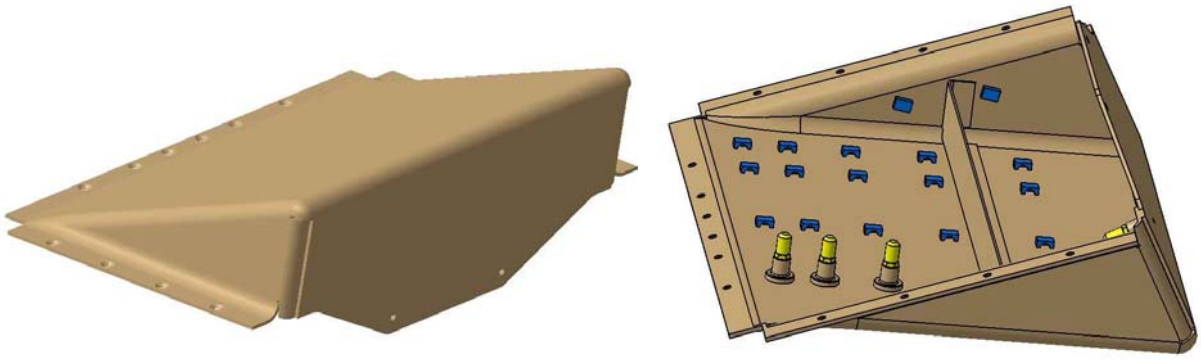

Figure 16: Mechanical design of C/SiC closed flap, fixation scheme, and thermocouple & pressure transducer integration; picture provided by SNECMA Moteurs.

The raw data consists of a series of grey-scale images and a mapping, which assigns an integration time to each image. The extraction of the external heat fluxes involved several steps, which will be discussed subsequently.

4.1 Image distortions

The payload compartments and thus the camera are attached to the internal structure of the vehicle. Due to vibrations and due to thermal expansion, the outer shell can move considerable relative to the camera. This potentially introduces lateral, rotational and perspective distortions between different images. Before comparing pixel-by-pixel intensities, these distortions have to be removed.

This is achieved by comparing the location of several reference points on the image to their nominal location. Reference points are structural features such as thermocouples and fixture points. The distortion can be uniquely determined from four such reference points. It is assumed that the flap surface is stiff, *i.e.*, that the distortion matrix is constant over the field of view. This assigns a flap coordinate to each pixel of the image.

4.2 CCD pixel correction and sensor temperature correction

The individual pixels of the CCD detector are not perfectly uniform. The behaviour of each pixel is known from a pre-launch calibration and the necessary correction can easily be applied. A second necessary correction involved the variable temperature of the CCD. A temperature sensor is placed near the sensor and this temperature is recorded by the DHU. The behaviour of the CCD with respect to its temperature is also supplied by the camera's manufacturer.

4.3 Integration time scaling

In order to make best use of the dynamic range of the camera, the integration time is adjusted based on the flap temperature (Sec. 2.4.3). The image intensity scales linearly with the integration time as long as the detector is not saturated. It is thus sufficient to linearly scale each image to an arbitrary reference integration time.

4.4 Averaging

The spatial resolution is governed by the thickness of the C/SiC structure (3 mm). Strong spatial gradients of the external heat flux are smeared out to produce less steep gradients of the internal temperature. The camera's resolution is sufficient to yield higher spatial resolution given a thinner structure. The same is true for the temporal resolution. While images are acquired at 30 Hz, the thickness of the structure and the thermal conductivity prescribes a diffusive time scale, which is significantly longer. If it is found to be necessary, temporal averaging over multiple images (after applying the corrections) and spatial averaging

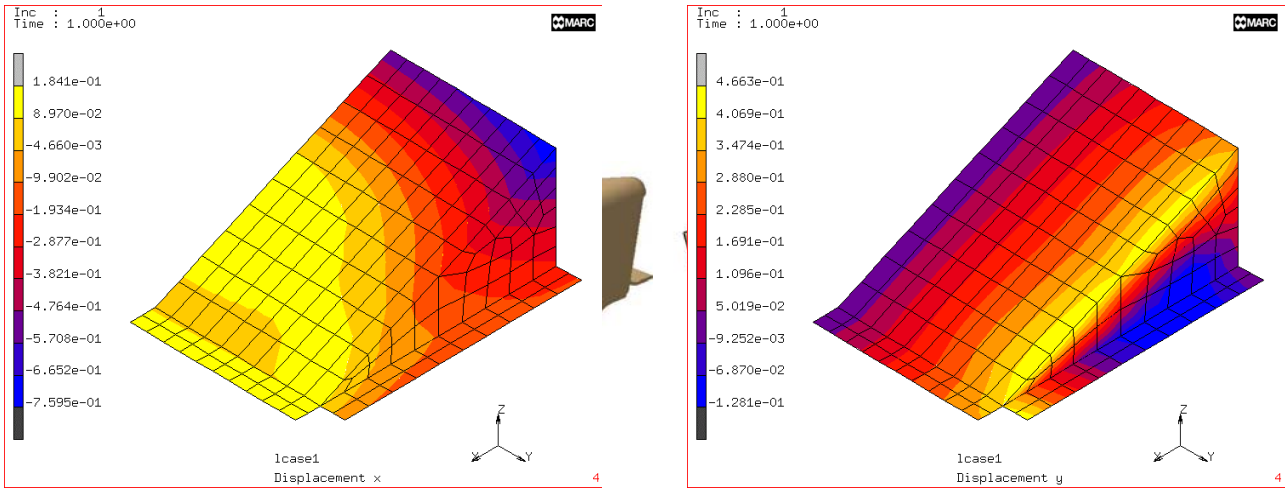

Figure 17: Lateral displacement in x- (left) and y-direction (right) due to thermal expansion assuming unconstrained boundary conditions; pictures provided by SNECMA Moteurs.

over multiple pixels can be employed without much loss of information.

4.5 Internal flap temperature

After applying the above-mentioned corrections, the temperature in the inside of the flap surface can be determined from the known sensitivity of the camera, the known emissivity of the C/SiC and the transmissivity of the neutral-density filter.

4.6 Inverse method

The inverse method is described in detail in Ref. [1] and the interested reader is referred there. The required inputs are the geometry of the structure and the thermal & radiative properties of the C/SiC. In order to account for radiation losses to the inside of the flap, the geometry and optical properties of this instrument compartment have to be known also. The result is the temporally and spatially resolved external heat flux over the field-of-view.

5.0 ALTERNATIVE DIAGNOSTIC TECHNIQUES

As mentioned in Sec. 3.0, thermographic phosphors were evaluated to provide redundant and supplementary two-dimensional temperature data. Rare-earth doped thermographic phosphors emit fluorescent light in the red visible region when excited in the blue and near-UV range of wavelengths. The lifetime of the fluorescence (order of tens of microseconds) is a function of the temperature and can be measured when a pulsed light source is used for the excitation. See Ref. [18] for an excellent introduction to the technique. Note that thermographic phosphors differ from so-called temperature-sensitive paints in that they are not organic molecules, which are only applicable up to ~150ºC.

This principle has been used for point-wise measurements of the temperature up to 1,800 K [20][21][22]. In point measurements, the fluorescence intensity decay can be resolved temporally. Adequate frame rates for two-dimensional detectors (such as CCD's) are not achievable as present. Instead, it was envisioned to acquire image frames at successive excitation pulses while varying the delay of the camera's shutter relative to the excitation pulse. Different temporal windows of the decay signal are thus acquired. By assuming a single-exponential decay, the fluorescence lifetime can be determined from the intensity ratio of two images.

A first design examined the possibility to place sapphire windows into the C/SiC structure, paint the exterior of the window while illuminating and observing from the inside and thus obtain temperature data directly from the capsule's exterior. While SNECMA Moteurs determined that windows can be accommodated, the mechanical properties of the coatings (phosphors plus ceramic binder) proved inadequate for high-speed flow applications.

Then we examined the possibility of coating the interior of the flap. The infrared camera would look at one half of the flap, while the thermographic phosphor coating would be applied to the other half, thus providing redundant temperature data. The advantage of lifetime imaging of thermographic phosphors over infrared thermography is that the former measures the temperature directly, because a fixed and known relationship between the decay rate (lifetime) and the temperature exists, whereas the unknown emissivity adds uncertainty for the latter.

This part of the SWBLI payload was dropped due to mass, power, cost, complexity constraints and because of the tight schedule.

6.0 SUMMARY AND CONCLUSIONS

We described a payload expected to fly in 2007, which will measure the surface heat flux on a control surface-like compression ramp spatially and temporally resolved (Figure 18). The payload combines classical thermocouples with state-of-the-art infrared imaging technology and data analysis algorithms. The payload includes a simple off-the-shelf data handling unit.

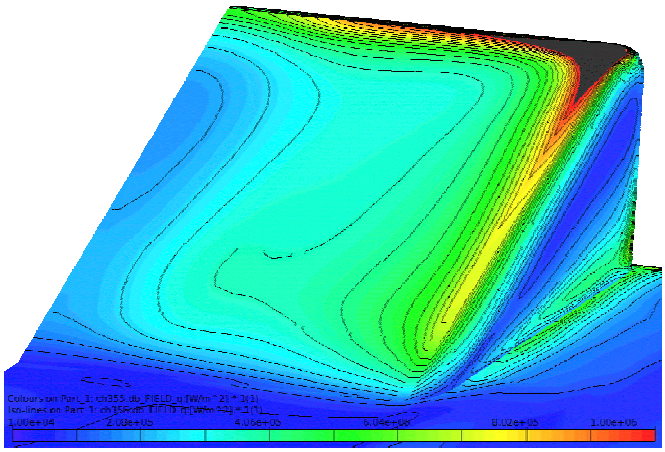

Figure 18: Predictions of surface heat flux assuming fully catalytic walls; provided by Jan Vos, CFS Engineering.

ACKNOWLESGEMENTS

The authors wish to acknowledge the contributions of their project partners, namely HTS AG, CFS Engineering, and SNECMA Moteurs and ONERA DMAE (Toulouse).

[1] Muylaert, J.-M. (2005). *EXPERT re-entry flight experiments*, RTO Lecture Series on Flight Experiments for Hypersonic Vehicle Development, Rhode-Saint-Genese (Belgium), Oct. 24-27.

[2] Nortershauser, D., Millan, P. (2000) *Resolution of a three-dimensional unsteady inverse problem by sequential method using parameter reduction and infrared thermography measurements*. Numerical Heat Transfer **37** (6):587-611.

[3] Liepmann, H.W., Roshko, A. (1957). *Elements of Gas Dynamics*. John Wiley & Sons, New York.

[4] Reijasse, P., Bur, R., Chanetz, B. (2001). *Experimental analysis of aerodynamic interactions occurring on hypersonic spacecraft*. Journal of Spacecraft and Rockets **38** (2):129-135.

[5] Hillier, R., Boyce, R.R., Creighton, S.A., Fiala, A., Jackson, A.P., Mallinson, S.G., Sheikh, A.H., Soltani, S., Williams, S. (2003). *Development of some hypersonic benchmark flows using CFD and experiment*. Shock Waves **12** (5):375-284.

[6] Settles, G.S., Dodson, L.J. (1994). *Supersonic and hypersonic shock boundary-layer interaction database*. AIAA Journal **32** (7):1377-1383.

[7] Benay, R., Chanetz, B., Delery J. (2003). *Code verification/validation with respect to experimental data banks*. Aerospace Science and Technology **7** (4):239-262.

[8] Lee, C.B., Wang, S. (1995). *Study of the shock motion in a hypersonic shock system turbulent boundary-layer interaction*. Experiments in Fluids **19** (3):143-149.

[9] Leyland, P. (1996). *Shock-wave/boundary-layer interactions at hypersonic speed by an implicit Navier-Stokes solver*. International Journal of Computational Fluid Dynamics **6** (1):71-87.

[10] Graur, I.A., Ivanov, M.S., Markelov, G.N., Burtschell, Y., Valerio, E., Zeitoun, D. (2003). *Comparison of kinetic and continuum approaches for simulation of shock wave/boundary layer interaction*. Shock Waves **12** (4):343-350.

[11] Henckels, A., Kreins, A.F., Maurer, F. (1993). *Experimental investigations of hypersonic shock-boundary layer interaction*. Zeitschrift für Flugwissenschaften und Weltraumforschung **17** (2):116-124.

[12] Chanetz, B., Pot, T., Bur, R., Joly, V., Larigaldie, S., Lefebvre, M., Marmignon, C., Mohamed, A.K., Perraud, J., Pigache, D., Sagnier, P., Verant, J.L., William, J. (2000). *High-enthalpy hypersonic project at ONERA*. Aerospace Science and Technology **4** (5):347-361.

[13] Davis, J.P., Sturtevant, B. (2000). *Separation length in high-enthalpy shock/boundary-layer interaction*. Physics of Fluids **12** (10):2661-2687.

[14] Coet, M.C., Chanetz, B. (1994). *Thermal effects in shock wave/boundary layer interactions in hypersonic processes*. Recherche Aerospatiale (4):251-268.

[15] Chanetz, B., Coet, M.C. (1993). *Shock-wave boundary layer interaction analyzed in R5CH laminar hypersonic wind-tunnel*. Recherche Aerospatiale (5): 43-56.

[16] Verma, S.B. (2003). *Experimental study of flow unsteadiness on a Mach 9 compression ramp interaction using a laser schlieren system*. Measurement Science and Technology **14**:989-997.

[17] Beck, J.V., Blackwell, B. (1985). *Inverse Heat Conduction*. Wiley-Interscience, New York.

[18] Cates, M., Allison, S.W. (2001). Phosphor Thermometry Tutorial. http://www.ornl.gov/sci/phosphors/Pdfs/tutorial.pdf

[19] Allison, S.W., Boatner, L.A., Gillies, G.T., (1995) *Characterization of high-temperature thermographic phosphors – spectral properties of LuPo4-Dy(1%), Eu(2%)*. Applied Optics **34** (25):5624-5627.

[20] Allison, S.W., Beshears, D.L., Gadfort, T. Bencic, T., Eldridge, J., Hollerman, W.A., Boudreaux, P. (2001). *High temperature surface measurements using lifetime imaging of thermographic phosphors: bonding tests*. In: Proceedings of the 19th International Congress on Instrumentation in Aerospace Simulation Facilities, NASA Glenn Research Center, Cleveland, OH, Aug. 27-30.

[21] Eldridge, J.I., Bencic, T.J., Allison, S.W., Beshears, D.L. (2004). *Depth-penetrating temperature measurements of thermal barrier coatings incorporating thermographic phosphors.* Journal of Thermal Spray Technology **13** (1):44-50.

[22] Allison, S.W., Gillies, G.T. (1997). *Remote thermometry with thermographic phosphors: Instrumentation and applications*. Review of Scientific Instruments **68** (7):1-36.